Journal of Alloys and Compounds 1009 (2024) 176900

Contents lists available at ScienceDirect

Journal of Alloys and Compounds

journal homepage: www.elsevier.com/locate/jalcom

Intermediate-spin state of Co ions in magnetic and thermoelectric properties of double perovskite Ba_2CoNbO_6

D.V. Popov [a,*], R.G. Batulin [b], M.A. Cherosov [b], I.V. Yatsyk [a], T.I. Chupakhina [c], Yu.A. Deeva [c], A.S. Makarchenko [a], D.I. Fazlizhanova [d], V.A. Shustov [a], R.M. Eremina [a], T. Maiti [e]

[a] Zavoisky Physical-Technical Institute, Federal Research Center "Kazan Scientific Center of RAS", Kazan 420029, Russia
[b] Kazan (Volga Region) Federal University, Kazan 420008, Russia
[c] Institute of Solid State Chemistry of the Russian Academy of Sciences (UB), Ekaterinburg 620990, Russia
[d] Skolkovo Institute of Science and Technology, Moscow 121205, Russia
[e] Department of Materials Science and Engineering Indian Institute of Technology, Kanpur 208016, India

ARTICLE INFO

Keywords:
Double perovskite
Thermoelectric
ESR
Spin-glass
Intermediate-spin state
Lowspin state

ABSTRACT

Double perovskite Ba_2CoNbO_6, obtained by pyrolysis of nitrate-organic mixtures, was studied by XRD, XRF, DFT, AC/DC-magnetization, specific-heat, thermoelectric, and ESR methods. The sample has cubic symmetry space group *Pm3m* with $a = b = c = 4.0074(11)$ Å. Deficiency in oxygen ions shows the presence of Co ions in both 3+ and 2+ valency. According to AC-magnetization and specific-heat data, Ba_2CoNbO_6 demonstrates spin-glass ordering at $T_{SG} = 30$ K at external field value of 0.1 kOe. This temperature of spin glass transition drops with field power increase down to complete suppression at 10 kOe. The effective magnetic moment determined using the Curie-Weiss approximation is 4.29 μ_B, which is consistent with the theoretical estimation for Co ions in the intermediate-spin state. The peak at $T = 90$ K, observed in the temperature dependence of the specific heat and accompanied by a peak in the ESR linewidth, is possibly due to the structural transition at this temperature. The Seebeck coefficient of the compound is $S = 4$–6.5 μV/K and the band gap obtained within the small-polaron-jump conductivity model is $\Delta E = 0.284$ eV in the temperature range of 350–550 K connected with DFT calculation. An intensity ESR line, related to Co^{2+} ions, was observed in ESR spectra.

1. Introduction

In the last decade, there has been an active search for stable thermoelectrics operating at high temperatures (in the region of ≈ 600 K). As it has been shown, the properties of thermoelectrics are influenced not only by the processes of diffusion of charge carriers and phonons, but also by the spin components. The MnTe features were studied in detail. In particular, it has been demonstrated that MnTe spins both in the ordered state of magnons and in the disordered paramagnetic state contribute to thermoelectric properties [1,2].

In paramagnetics, the spin moments are considered to be completely disordered, however, this consideration is not quite correct. Spins in paramagnetics tend to create short-living local structures, referred to as the paramagnons. The effective lifetime of a single paramagnon is several nanoseconds, but even during such a short period of time, a paramagnon, provided that it is located in a temperature-gradient zone, can move and drag along free electrons (the so-called magnon-electron drag, or MED), thus inducing thermo-EMF. The magnitude of thermo-EMF can be determined via measurements of thermoelectric properties, namely the Seebeck coefficient *S* [3,4].

Recently, great interest in double perovskites has been attracted by the possibility of their use as thermoelectrics. The Seebeck coefficient *S* was measured for multiple Ba-based double perovskites at various temperatures. Specifically, for $Ba_xSr_{2-x}TiMoO_6$ (x = 0, 0.1, 1, and 2) and $Ba_xSr_{2-x}Fe_{0.5}Mo_{0.5}O_6$ (x = 0.1 and 0.2) it slowly and almost linearly decreases from 3 μV/K at 400 K down to − 12μV/K at 1200 K [10,11]. For Ba_2InTaO_6, the Seebeck coefficient exponentially drops from −80 to −180 μV/K in the T=100–600 K range, but at T=600 K it reaches saturation and remains constant up to the measurement limit of 1000 K [12]. In Ba_2FeMoO_6, the opposite behavior is observed: the values of the Seebeck coefficient increase with temperature from − 2700μV/K at 200 K up to 0 μV/K at approximately 900 K [13]. However, the band gap of both Ba_2InTaO_6 and Ba_2FeMoO_6 is significantly higher than usual for semiconductors.

* Corresponding author.
E-mail address: Kazan-city.dvpopoff@yandex.ru (D.V. Popov).

https://doi.org/10.1016/j.jallcom.2024.176900
Received 27 June 2024; Received in revised form 23 August 2024; Accepted 5 October 2024
Available online 9 October 2024

The Ba_2CoNbO_6 double perovskite properties were studied in several papers [5,6,9]. According to them, Ba_2CoNbO_6 features a cubic structure *Pm3m* ($a = 4.06$ Å) with random distribution of Co^{3+} and Nb^{5+} ions in corresponding positions [5]. It was found that this compound has a magnetic transition at $T = 45$ K [6]. The authors observed that below the transition temperature, the compound exhibits behavior typical of canted antiferrmagnetics. The magnetic transition is completely suppressed by the external field at $H = 50000$ Oe, possibility due to the formation of spin glass. However, no AC-magnetization measurements have been carried out to clarify this effect.

The effective localized moment calculated via the Curie-Weiss-law approximation has values of 3.39–4.09 μ_B, that, according to the authors, indicates the presence of intermediate-spin Co^{3+} ions in the compound and that the competition between high-spin ($S = 2$) and intermediate-spin ($S = 1$) Co ions interactions may lead to the formation of spin glass.

The presence of two magnetic ions in the pervoskite structure can lead to unusual magnetic phenomena. The mixed-valence state of Ni and Mn ions in La_2NiMnO_6 have determined magnetic properties, where the monoclinic phase has shown ferromagnetic transition near 280 K, and the orthorhombic phase has shown weak ferro/antiferromagnetic spin ordering temperature around 150 K [7]. Substitution of lanthanum ions with other rare earth ions, for example, Sm and Yb doping at the La sites of La_2NiMnO_6, decreased T_C and the presence of an additional weak magnetic transition at low-temperature range (~ 100–150 K) [8]. Therefore, the presence of only one magnetic ion makes the magnetic picture in double perovskites simpler.

However, the transport, thermoelectric, and detailed magnetic and magnetic-resonance properties have not been studied. The goal of our research is to experimentally study the aforementioned magnetic and transport properties of double perovskite Ba_2CoNbO_6.

2. Sample preparation

Depending on the synthesis method, cobalt ions and niobium ions can form chains and planes, or be located randomly. In previous studies the samples have been prepared by the solid-state reaction method with the starting materials being $BaCO_3$ (4N, Soekawa), Co_3O_4 (3N, High Purity Chem. Lab.), and Nb_2O_5 (4N, Soekawa) [6].

In the present work, the sample of the composition Ba_2CoNbO_6 was synthesized by the method of pyrolysis of nitrate-organic compositions, followed by annealing of the resulting reaction mixture in air at 1100°C-1250°C. $Ba(NO_3)_2$ (barium nitrate), Nb_2O_5 (niobium oxide V), and $Co(NO_3)_2{*}6H_2O$ (cobalt (II) nitrate) were used as starting reagents. Polyhydric alcohol xylitol was used to partially dissolve niobium oxide and played a role of an organic fuel to transfer the process to the solution combustion regime. Barium nitrate was dissolved in distilled water and a stoichiometric amount of xylitol was added to the solution to convert barium nitrate into the state of a complex compound in order to avoid the precipitation of insoluble barium salts when mixed with a solution of other reagents. Cobalt II nitrate was dissolved in distilled water. Both solutions were mixed and ammonium hydroxide (NH_4OH) was added until the acid was neutralized, and the pH value reached 12.5. The solution was left for a day, then xylitol was added in excess (2:1) compared to the stoichiometric amount. Afterward, the reaction mixture was heated at 460 °C. The solution was evaporated at this temperature until it ignited and a black nanodispersed powder was formed. The powder was calcined at 950 °C for 6–8 h until carbon was removed, then pressed into tablets and sequentially, with intermediate grinding and repressing, annealed at 1000 °C, 1050 °C, 1100 °C, and 1200 °C for 8 h.

3. Experimental setup

The X-ray diffraction pattern of the sample was collected using the DRON-7 diffractometer with 0.02 ^{o} steps in the 5–100 ^{o} range and processed via the FULLPROF 2018 software.

The X-ray fluorescence analysis was performed on the Bruker S2 Ranger X-ray fluorescence spectrometer to determine the ion content in the sample. The oxygen volume in the sample was established using the thermogravimetry (TG) method on the Setagram TG-92 analyzer.

DC- and AC-magnetization, $M(H)$-dependence, and specific-heat measurements were performed via the PPMS-9 device. DC magnetization was measured in the temperature range of 5–300 K at the magnetic fields of 0.1 and 1–10 kOe in both zero-field cooling (ZFC) and magnetic-field cooling (FC) regimes. Magnetization hysteresis loops were measured at temperatures of 5, 10, 30, 50, 150, and 300 K at the external magnetic fields of ± 3 T. Specific heat was measured in the temperature range of 5–300 K at the external magnetic fields of 0 and 9 T.

ESR measurements were performed using a Bruker ELEXSYS E500-CW spectrometer equipped with continuous-flow He and N_2 cryostats. Measurements were performed in the X-band with a frequency of 9.4 GHz, a temperature range of 5–340 K, and a magnetic-field range of 0–1.4 T.

The temperature dependence of the Seebeck coefficient of Ba_2CoNbO_6 samples in contact with platinum was measured in air within the temperature range of 350–550 K using a home-built device. Measurements were performed at a temperature gradient of 30 K at the edges of the sample.

To perform density-functional-theory calculations, we employed the Quantum Espresso code with norm-conserving pseudopotentials [14,15]. The kinetic energy cutoff of 90 Ry was chosen, and a 12 × 12 × 6 k-grid was used for the conventional unit cell consisting of 20 atoms.

To capture the localized nature of 3*d* orbitals of transition metals, we applied the ACBN0 exchange-correlation functional approximation [16], as implemented in the AFLOW*π* software [17]. This method allows a self-consistent calculation of the Hubbard correction in the DFT+U approximation for all crystallographically non-equivalent positions independently.

We examined two configurations of transition metals in the structure, as shown in Fig. 1. In the first configuration, there is a uniform distribution where the nearest transition metal to niobium is cobalt and vice versa. In the second configuration, layers of cobalt are interchanged with layers of niobium.

Also, we employed variable cell relaxation. The atomic positions were relaxed until the remaining forces were less than 10^{-3} Ha/Bohr, which is approximately 0.05 eV/Å, and the difference in total energies between two self-consistent cycles was less than 10^{-4} Ha.

4. Results and discussion

4.1. X-ray diffraction and X-ray fluorescence analysis

X-ray diffraction patterns (Fig. 2) were approximated by a lattice with the cubic space group *Pm3m* with crystallographic parameters $a = b = c = 4.0074(11)$ Å. This lattice is similar to the previous results with the cubic structure *Pm3m* and $a = b = c = 4.06$ Å [5]. The fitting parameters are shown in Table 1. The crystallography parameters with the fitting errors are presented in Table 2.

Using X-ray fluorescence analysis, we determined that the compound has 2(0.03) ions of Ba, 1(0.03) ion of Nb and 0.998(0.03) ions of Co per unit cell. From X-ray diffraction pattern approximation it was established, that oxygen occupation is 5.9 per unit cell. Therefore, to correspond to the electroneutrality in the sample, Co ions must be divided into two categories by valency: Co^{3+} occupies approximately 0.8 and Co^{2+} occupies the remaining 0.2 of all Co positions. Additionally, through XRF analysis the presence of impurities was observed, such as Al (0.17 %), Si(0.37 %), Ca(0.04 %), Fe(0.05 %) and Zn(0.03 %), most likely due to melting or destruction of the crucible during sample preparation. TG method showed an oxygen volume of 6(0.03) ions per unit cell.

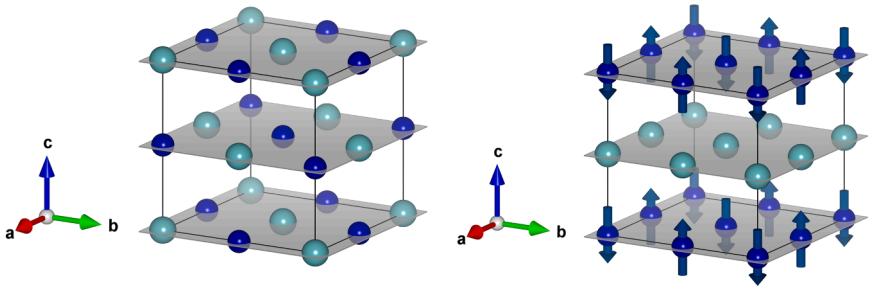

Fig. 1. Various distributions of Co/Nb in Ba_2CoNbO_6: with (left) Co and Nb being distributed uniformly and with (right) layers of Co and Nb being interchanged. Cobalt ions are shown by blue spheres, niobium ions are shown by green spheres. Arrows (right picture) show the direction of the spin of the cobalt ions.

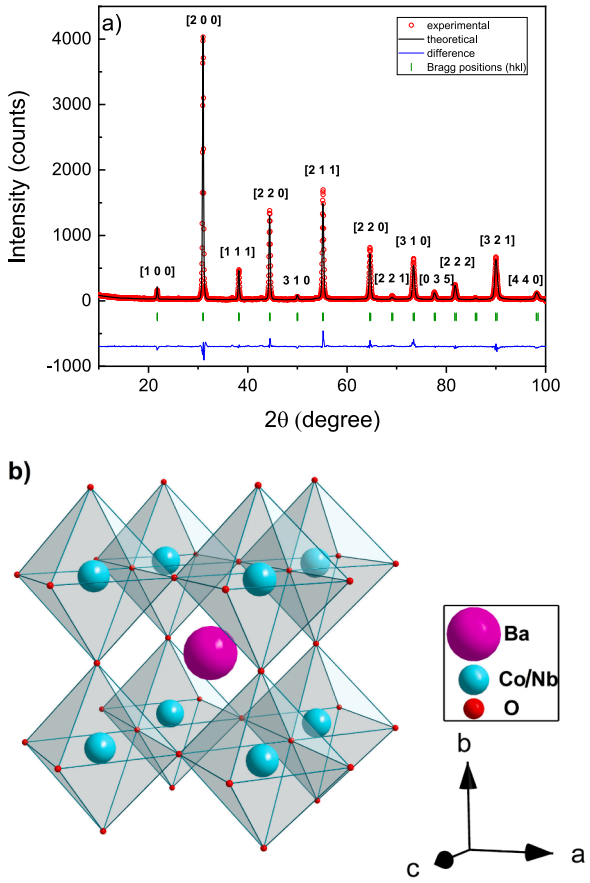

Fig. 2. a) The diffraction patterns of double perovskite Ba_2CoNbO_6: experiments (red dots), calculations (black line), and their difference (blue line). b) The structure of the Ba_2CoNbO_6 compound.

Table 1
The unit cell parameters, interatomic distances and reliability factors of the Ba_2CoNbO_6 double perovskite.

$a = b = c$ (Å)	4.0074(11)
V (Å^3)	67.790(3)
Co/Nb-O (x6) (Å)	2.0387(1)
Ba-O (x12) (Å)	2.8832(1)
χ^2 (GoF) (Å)	1.5
Rf-factor (Å)	6.59
Bragg R-factor (Å)	8.13
R_p (Å)	9.54
R_{2p} (Å)	13.0
R_{exp} (Å)	10.63

4.2. DFT analysis

The relaxation of the monoclinic structure resulted in a transition to a cubic structure, indicating the thermodynamic instability of the monoclinic phase. We didn't analyze the thermodynamic stability of various distributions of Co/Nb since magnetic measurements indicate disorder (Fig Fig 3).

To determine the spin states, Löwdin partitioning was performed. For further analysis, we assumed that Ba, O, Nb, and Co are in the 2+, 2-, 5+, and 3+ oxidation states, respectively. In this scenario, charge neutrality is satisfied, and each element is in its stable oxidation state. Nb in the 5+ oxidation state is non-magnetic, so all magnetism originates from Co. Co in the 3+ oxidation state may be in a high-spin state with $S = 2$, an intermediate-spin state with $S = 1$, or a low-spin state with $S = 0$. We associate Löwdin magnetic moments of 0.5–0.6 with $S = 0$, 1.5 with $S = 1$ and 2.7 with $S = 2$.

Despite considering spin polarization and specifying the initial spin distribution, the calculation revealed that, when Co and Nb are uniformly distributed, Co $3d^6$ is in the low-spin state with spin $S = 0$. Consequently, the entire system turns out to be non-magnetic in this atomic configuration.

When Co layers are interchanged with Nb layers, we converged two magnetic structures. In the first structure, high-spin Co is antiferromagnetically ordered. In the second structure, one Co ion is in a low-spin state, while the other is in an intermediate-spin state. The antiferromagnetic structure is 0.01 eV/atom more energetically favorable than the structure with Co in mixed low-spin and intermediate-spin states.

The results of calculating the density of states projected onto atomic orbitals are presented in Fig. 3. The outcomes differ significantly: the structure with a uniform distribution has a near-dielectric properties with a calculated band gap of 1.8 eV, whereas the structure where layers of Co and Nb are interchanged is a narrow-gap semiconductor.

4.3. Magnetization measurements

Fig. 4 shows the magnetic susceptibility temperature dependence measured at 0.1, 10 and 100 kOe. The ZFC and FC curves diverge at low external magnetic fields of 0.1 and 1 kOe. They are separated at $T = 30$ K and 0.1 kOe, but at 1 kOe the separation temperature drops down to $T = 15$ K. Moreover, at $H = 10$ kOe, no discrepancy is detected. Clearly visible are the local peaks at $T_{SG} \approx 30$ K. The inverse magnetic susceptibility was approximated using the Curie-Weiss law

$$\chi = \frac{C}{T - \Theta_{CW}}, \quad (1)$$

where C is the Curie constant and Θ_{CW} is the Curie-Weiss temperature. The deviation from the Curie-Weiss law approximation is occurs at $T \approx 90$ K.

The fitting parameters are shown in Table 3. The Curie-Weiss temperature is negative, therefore indicating the presence of antiferromagnetic interaction between the spins in the sample, similarly to the

Table 2
The crystallographic positions in the Ba_2CoNbO_6 double perovskite.

Atom	Site	Wyck.	x	y	z	B11	B22	B33	Occupancy
Ba	m−3m	1b	0.5	0.5	0.5	−0.016(2)	−0.016(2)	−0.016(2)	1
Co	m−3m	1a	0	0	0	−0.037(7)	−0.037(7)	−0.037(7)	0.5
Nb	m−3m	1a	0	0	0	−0.037(7)	−0.037(7)	−0.037(7)	0.5
O	4/mm.m	3d	0.5	0	0	−0.073(2)	−0.043(3)	−0.043(3)	2.95(3)

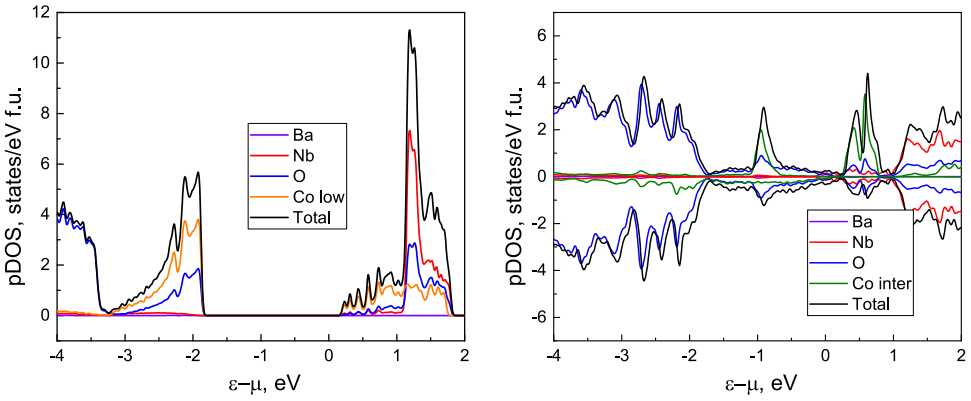

Fig. 3. Density of states projected onto atomic orbitals: (violet lines) 6s Ba orbitals, (green lines) 3d orbitals of Co in the intermediate-spin state, (orange lines) 3d orbitals of Co in the low-spin state, (red lines) 3d Nb orbitals, and (blue lines) 2p O orbitals when (left) Co and Nb are distributed uniformly and when (right) the layers of Co and Nb are interchanged. Also shown by black lines is the total density of states.

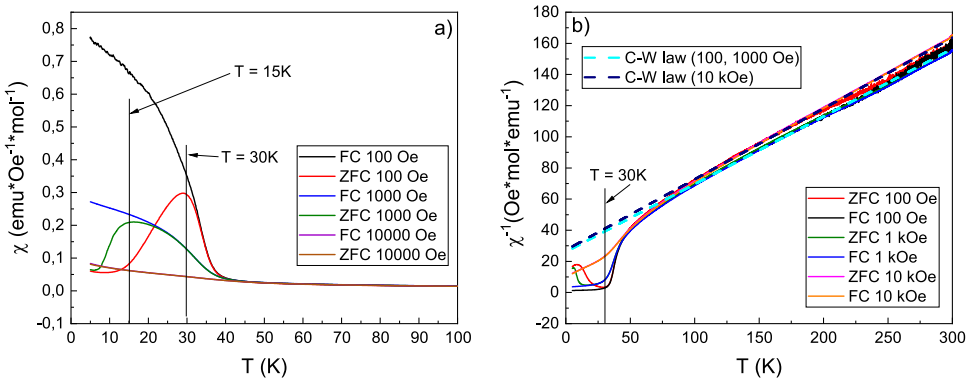

Fig. 4. (a) The magnetic susceptibility and (b) the inverse magnetic susceptibility of Ba_2CoNbO_6 at 0.1, 1, and 10 kOe in ZFC and FC regimes. The Curie-Weiss-law fit is shown by dashed lines.

Table 3
The Curie constant, Curie-Weiss temperature, and effective magnetic moments of Ba_2CoNbO_6 ceramics.

H(Oe)	T_{SG} (K)	Θ_{CW} (K)	C (K · emu/mol)	$\mu_{eff}(\mu_B)$
100	30	–60(2)	2.3(0.13)	4.29(0.13)
1000	15			
10000	–		2.2(0.13)	4.19(0.13)

other Ba-based double perovskites [6,18]. The experimental effective magnetic moments were calculated as

$$\mu_{\text{eff}} = \sqrt{\frac{3k_B \cdot C}{N_A}}, \tag{2}$$

where N_A is the Avogadro constant and k_B is the Boltzmann constant. The theoretical effective magnetic moment is calculated as

$$\mu_{\text{eff}}^{\text{Theor}} = g \cdot \sqrt{N \cdot S(S+1)} \cdot \mu_B, \tag{3}$$

where $N = 0.998$ for Co^{3+}, according to the X-ray fluorescence analysis, μ_B is the Bohr magneton, S is the spin, and g is the g-factor.

Firstly, we calculated the theoretical effective moment under the assumption that the cobalt ions occupy Co positions as 0.8 for Co^{3+} and 0.2 for Co^{2+}; Co ions of both valency are in a high-spin state with $S = 2$ and $S = 3/2$, respectively; g-factor is for Co ions $g = 2$. In this case, the experimental magnetic moment is significantly lower than the calculated one, being 4.29 μ_B against 4.711 μ_B. This inconsistency proves the idea of Co ions being in different spin-state [19–21], that was established through our DFT calculations. If Co^{3+} is presented at intermediate-spin state ($S = 1$) according DFT calculation, theoretical effective magnetic moment value drops down to 3.07 μ_B. However, the assumption of $g = 2$ is quite arbitrary. Therefore, below we present the EPR-spectra measurements, which we will use for a more correct description of the experimental effective g-factor. The theoretical effective magnetic moments are shown in Table 3. If we use the effective g-factor value from the ESR data $g = 3.25$ for Co^{3+} and $g = 2.1$ for Co^{2+} as in $Sr_2CoNbO_{6-\delta}$ [22] then we get that 84 % of cobalt 3+ ions are in an intermediate spin state ($S = 1$). This corresponded to our DFT

calculations for the antiferromagnetic structure where layers of Co and Nb are interchanged. We conclude that, with an accuracy of 4 %, the sample under study contains 80 % Co^{3+} ions and 20 % Co^{2+}. This falls into the error of determining the oxygen concentration from the X-ray and thermogravimetry analysis.

In the work [6] the Curie-Weiss temperature and the effective magnetic moments were obtained as a range of 50–60 K and 3.79–4.09 μ_B, respectively, meaning a high error level (about 7 %). The values exposed in the present work are $\Theta_{CW} = -60.2$ K and $\mu_{eff} = 4.29\mu_B$, which are close to the high-end values of the previously obtained ranges.

AC magnetization was measured in the temperature range $T = 15$–40 K and in the frequency range of 30–9998 Hz and an external magnetic field value of 0.735 Oe. A small shift was observed in the peak values around 30 K at different frequencies for both real and imaginary parts (Fig. 5). The Mydosh parameter, calculated from the real-part peak-shifts as

$$\Omega = \frac{T_2 - T_1}{T_2(log\nu_2 - log\nu_1)}, \tag{4}$$

is $\Omega = 0.00903$. This value is typical for the canonical spin glass [23].

At temperatures above 50 K, magnetization varies linearly with the magnetic field. Slight hysteresis loops are observed at 5 and 10 K. Their origin is possibly due to the presence of magnetic clusters or canted spins in the sample (Fig. 6). Changes in the form of the lines at $T = 5$, 10, and 30 K, manifested at $B \approx 0$ T, are characteristic of single-domain particles. These lines were approximated by the sum of paramagnetic and single-domain particle contributions as

$$M = \frac{2B_S}{\pi} atan\left(\frac{H}{H_T}\right) + \chi H, \tag{5}$$

where B_S is the saturation magnetization and H_T is the internal local one-axis anisotropy field [24]. The fit results are shown in Table 4.

4.4. Specific-heat measurements

Specific-heat temperature dependencies, measured at external magnetic fields of 0 and 9 T, are shown in Fig. 7. We describe them by the sum of lattice and magnetic contributions. The lattice contribution to specific heat is defined as

$$C = \alpha_D C_D + \sum_i \alpha_{E_i} C_{E_i}, \tag{6}$$

where C_D is the Debye specific heat term and C_E are the Einstein specific heat terms. These terms can be calculated as:

$$C_D = 9R\left(\frac{T}{\Theta_D}\right)^3 \int_0^{\frac{\Theta_D}{T}} \frac{x^4 e^x dx}{(e^x - 1)^2}, \tag{7}$$

$$C_E = 3R\left(\frac{\Theta_E}{T}\right)^2 \frac{exp(\frac{\Theta_E}{T})}{\left[exp(\frac{\Theta_E}{T}) - 1\right]^2}, \tag{8}$$

where Θ_D is the Debye temperature and Θ_E is the Einstein temperature. From experimental data, we determined the Debye and Einsten temperatures and the contribution ratio α (Table 5). The lattice contribution to the specific heat is shown by the red line in Fig. 7a. The magnetic contribution features a local peak at $T = 30$ K (Fig. 7a), similar to the magnetization measurements. An additional small peak is clearly visible at $T \approx 90$ K (inset on Fig. 7a). In the magnetization measurements, a deviation of inverse magnetic susceptibility from the linear Curie-Weiss law occurs at the same temperature (see Fig Fig 4a).

As can be seen from Fig. 7, the magnetic contribution has three peaks. At low temperatures, the position of the maximum depends on the magnetic field, while at $T = 30$ K and 90 K, it almost does not depend on the magnetic field.

The magnetic contribution may shed light on the above-mentioned problem of Co ions valency and possible spin-state variations. We calculate the theoretical magnetic contribution as [25]:

$$C(T,H) = \int_0^{2\pi} \frac{\sum_{i=1}^{m}\sum_{j=1}^{m}(\varepsilon_i - \varepsilon_j)^2 exp\left(\frac{-\varepsilon_i - \varepsilon_j}{kT}\right)}{kT^2\left(\sum_{k=1}^{m} exp\left(\frac{-\varepsilon_k}{kT}\right)\right)} sin\theta d\theta, \tag{9}$$

where ε are the eigenvalues of the Hamiltonian

$$H = g_{\parallel}\mu_B H_z S_z + g_{\perp}\mu_B(H_x S_x + H_y S_y) + DS_z^2 + E(S_x^2 - S_y^2), \tag{10}$$

where D and E are the parameters of the crystal field [26].

The calculations imply parallel and perpendicular g-factor values, obtained from the ESR measurements, and the ratio of Co ions with different valence, obtained from the effective-magnetic-moment calculations (Fig. 7b). For Co^{3+} in the intermediate-spin state ($S = 1$), the crystal-field parameters are $D = 5.5$ K and $E = 2.5$ K, and the g-factor values are $g_{\parallel} = 4.5$ and $g_{\perp} = 2$. The obtained values of crystal-field parameters D and E are consistent with the existing data and may vary from one compound to another. For Co^{II}-Y^{III}, D is positive and above 40 cm^{-1} and E is about 1.5–2 cm^{-1} [27] for $S = 3/2$. However, in [28], measurements for $Co(PPh_3)_2Cl_2$ yielded values of $D = -14(3)$ cm^{-1} and $E = 0.96(20)$ cm^{-1} for $S = 3/2$ as well. In [29], $LaAlO_3$ doped with Co^{3+} had $D = 2.1$ eV and $E = 0.8$ eV.

4.5. Thermoelectric measurements

The measured temperature dependencies of the Seebeck coefficient and the resistance are shown in Fig. 8a. The Seebeck coefficient of Ba_2CoNbO_6 gradually grows by approximately 50 %, from 4 μV/K at 350 K up to 6.5 μV/K at 550 K. These behavior and values are typical for

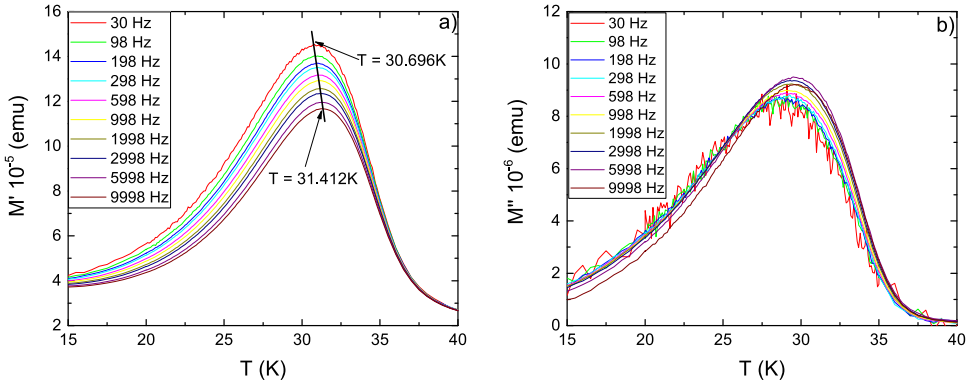

Fig. 5. (a) Real and (b) imaginary parts of the AC magnetization in Ba_2CoNbO_6.

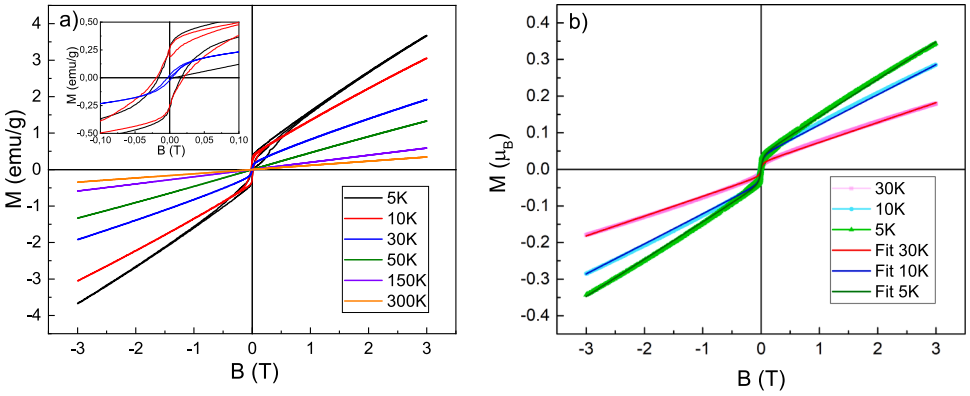

Fig. 6. (a) Hysteresis loops of Ba_2CoNbO_6 (Inset is a resized version) and (b) their fits at $T = 5$, 10, and 30 K.

Table 4
Approximation parameters of hysteresis loops of Ba_2CoNbO_6.

T(K)	B_S (μ_B)	H_T (Oe)	χ 10^{-6} (μ_B/Oe)
5	0.042		10.2
10	0.4	250	8.2
30	0.2		5.4

various chalcogenides [30] and perovskites [10,11]. The resistance was studied in the temperature range of 310–510 K (the inset in Fig. 8a). Using the results of these measurements, we calculated the band gap in the approximation of hopping conductivity of a small polaron (Fig. 8b) using the following equation:

$$\sigma = \frac{A}{T} exp\left(-\frac{\Delta E}{k_B T}\right) + Const \tag{11}$$

where A is the constant, ΔE is the band gap, and k_B is the Boltzmann constant. The obtained band gap is $\Delta E = 0.284$ eV. This value is similar to ones determined for Ba_2InBiO_6 ($\Delta E = 0.125$ eV) and Ba_2TlSbO_6 ($\Delta E =$ 0.307 eV) [31]. The band gap with this low value agrees with DFT calculations, as the layered structure of Co and Nb ions exhibits similar properties.

4.6. ESR measurements

The ESR lines were collected in the temperature range of 5–340 K. ESR lines at temperatures above 140 K have low resolution and have not been fitted. However, from the these lines it is obvious, that g-factor of the Ba_2CoNbO_6 compound is approximately 3.25 at temperatures above 90 K. The view of ESR spectra is shown in Fig. 9.

The spectra obtained look very similar to the ESR lines for another Co-containing double perovskite $Sr_2CoNbO_{6-\delta}$ [22]. In $Sr_2CoNbO_{6-\delta}$ Co ions have valency of 2+. As Co^{3+}, especially in intermediate-spin state, usually doesn't give any contribution in the ESR spectra with D and E crystal fields parameters, which were obtained from magnetic part of specific heat, it is save to say, that only Co^{2+} ions effects were obtained for Ba_2CoNbO_6, in similarity with [22]. However, a small additional line is observed for Ba_2CoNbO_6 at low temperatures of 5–15 K (Fig. 9a, inset), that was absent in $Sr_2CoNbO_{6-\delta}$. The similar line is also observed at temperatures around 117 K. Both of said lines have the same g-factor value of 2.1, that is the same value, that was obtained for $Sr_2CoNbO_{6-\delta}$.

ESR lines were approximated using the following equation:

$$\frac{dP}{dH} = \frac{d}{dH}\left(\frac{\Delta H + \alpha(H - H_{res})}{(H - H_{res})^2 + \Delta H^2} + \frac{\Delta H + \alpha(H + H_{res})}{(H + H_{res})^2 + \Delta H^2}\right), \tag{12}$$

where H_{res} is the resonance-line position, ΔH is the line-width, and α is the asymmetry parameter [32]. The line-width, intensity, and g-factor, inferred from the fitting procedure, are shown in Fig. 10 for one more intensity line in this compound. However, the parameters behavior changes with temperature. The ESR line is wide and has a relatively high

Table 5
The Debye and Einstein temperatures and the contribution ratio for Ba_2CoNbO_6.

	Θ (K)	α
Debye	180	1
	195	3
Einstein	410	2
	600	4

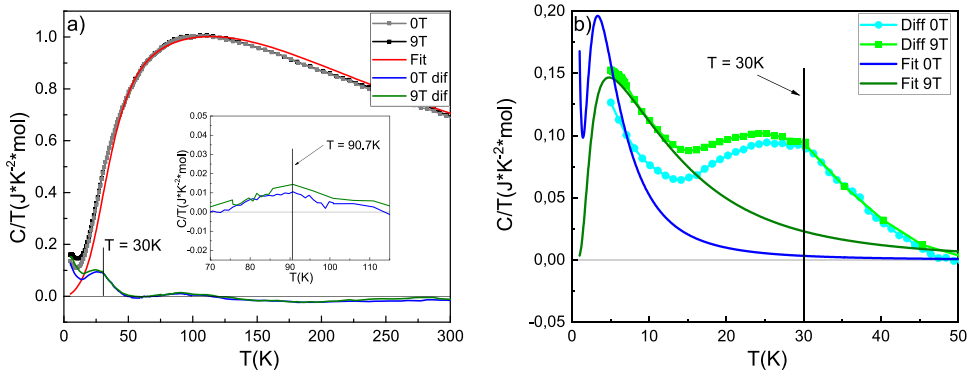

Fig. 7. (a) Temperature dependencies of the specific heat of Ba_2CoNbO_6. The sum of the Debye and Einstein contributions are shown by red line and the calculated magnetic contribution at magnetic fields of 0 T and 9 T lines is shown by blue and green lines, respectively. The inset shows a local peak in the magnetic contribution at $T = 90$ K. (b) The magnetic-contribution fits at different magnetic-field values.

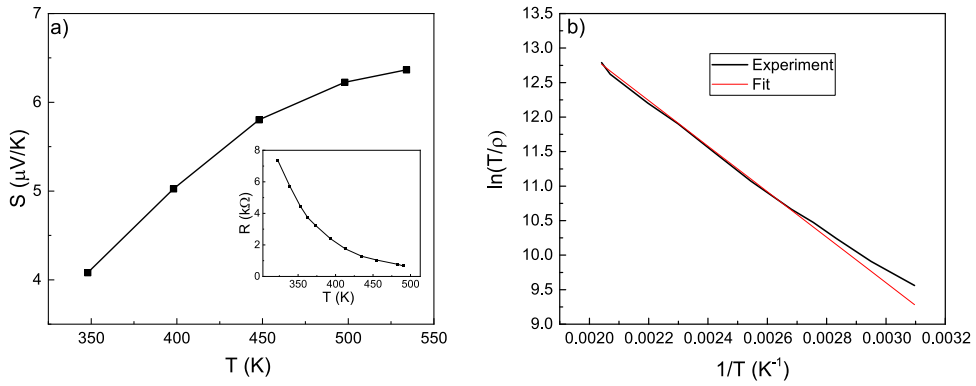

Fig. 8. Thermoelectric measurements: (a) the Seebeck coefficient and (b) the linear fit of the resistivity. The inset shows the resistance as a function of temperature.

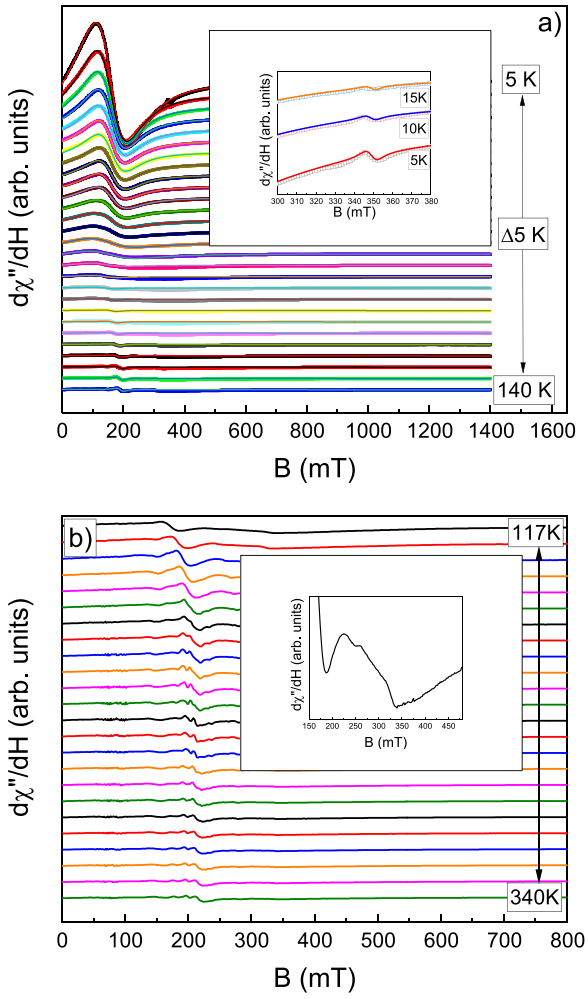

Fig. 9. The ESR lines of Ba_2CoNbO_6. a) $T = 5$–140 K with fits b) $T = 117$–340 K. Inset on a) shows small additional line at low temperatures. Inset on b) shows the same additional line at higher temperature.

intensity at temperatures below 90 K, while it is narrow and low-intensity at temperatures above 90 K. The main difference in the line behavior is the *g*-factor – at low temperatures it gradually increases from 4.2 at 5–55 K to 4.85 at 90 K, while at high temperatures it drops from 4.2 at 90 K to 3.5 at 140 K. Similar behavior was observed in previous studies of Co-containing compounds [19,33]. These features may indicate differently-oriented *g*-factors with $g_{\parallel} > g_{\perp}$ [34].

The inverse intensity was approximated via the Curie-Weiss law at

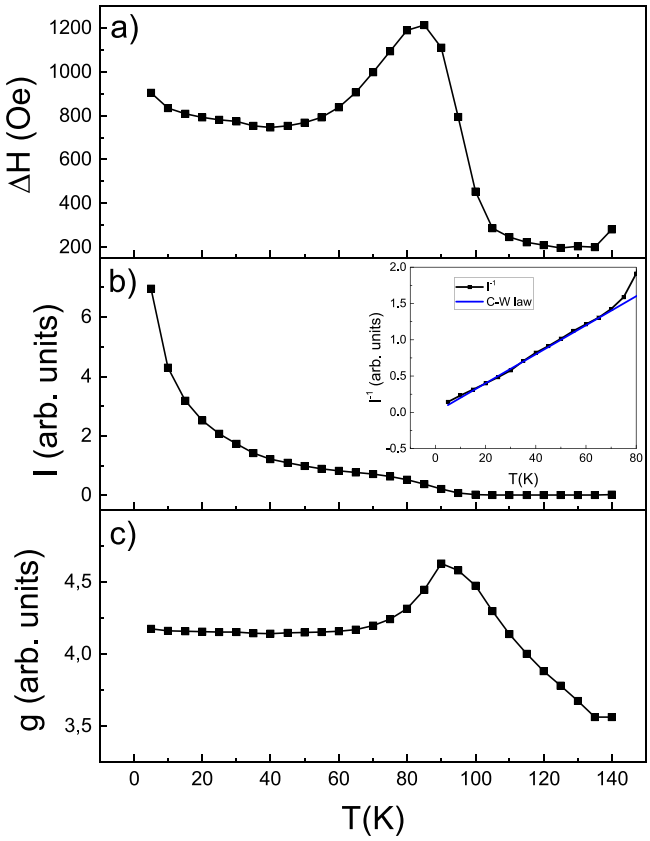

Fig. 10. Ba_2CoNbO_6 ESR line parameters: the (a) line-width, (b) intensity, and (c) *g*-factor. The inset shows a Curie-Weiss-law fit of the inverse intensity.

temperatures below 90 K. The Curie-Weiss temperature $\Theta_{CW}^{(I)}$ is 0 K, which means that some subsystem with Co^2 remains paramagnetic even at temperatures approaching absolute zero.

The line-width and *g*-factor show a local peak at $T \approx 90$ K, which is similar to the peak observed in specific-heat measurements and are probably associated with a structural phase transition in the sample.

5. Conclusion

The double perovskite Ba_2CoNbO_6 was studied through XRF, XRD, DFT, AC- and DC-magnetization, specific-heat, thermoelectric, and ESR measurements. The X-ray diffraction analysis showed, that the compound Ba_2CoNbO_6 has *Pm*3*m* space group ($a = b = c = 4.0074(11)$ Å), as well as deficiency in oxygen ions, indicating the presence of Co^{2+} ions in

the compound in a quantity of around 0.2. The DFT calculations showed the presence of low- and intermediate-spin-state Co^{3+} ions as well as layered ordering of Co and Nb ions. Two transitions are observed in the sample: one is associated with structural changes at a temperature of 90 K, which is reflected in the peak in the heat capacity. A striking characteristic of the structural changes is the sharp change in the temperature behavior of the EPR spectrum at 90 K. It should be noted that it is at this temperature that a deviation from the Curie-Weiss law from the experimental inverse magnetic susceptibility is observed. Another transition is observed at 30 K in weak magnetic fields. As Mydosh parameter Ω is 0.00903, the compound has spin-glass ordering at that temperature. With an increase in the applied magnetic field, the transition in the spin glass state shifts to low temperatures and is observed at 15 K in a magnetic field of 1000 Oe, and is suppressed in a magnetic field of 10 kOe. The Curie-Weiss temperature for the inverse magnetic susceptibility is $\Theta_{CW} = -60$ K. The effective magnetic moment, calculated by the Curie-Weiss-law approximation, is 4.29 μ_B, confirming the presence of intermediate-spin-state Co^{3+} ions. The calculated theoretical magnetic moment matches the experimental one, taking into account g-factor values and Co ions valency distribution and spin states, obtained from the various measurements performed. The magnetic contribution to the specific heat allowed us to calculate the crystal-field parameters $D = 5.5$ K and $E = 2.5$ K for cobalt ions. Thermoelectric measurements show the increase in the Seebeck coefficient with temperature from $S = 4\mu$V/K at $T = 350$ K to $S = 6.37\mu$V/K at $T = 534$ K. The band gap, obtained by the linear fit of resistivity, is $\Delta E = 0.284$ eV. and are probably associated with a structural phase transition in the sample. This is consistent with DFT calculations that showed the structure where layers of Co and Nb are interchanged and it is a narrow-gap semiconductor.

CRediT authorship contribution statement

D.V. Popov: Writing – original draft, Visualization, Formal analysis. **T. Maiti:** Validation, Project administration, Funding acquisition, Conceptualization. **M.A. Cherosov:** Investigation. **R.G. Batulin:** Investigation, Data curation. **T.I. Chupakhina:** Resources, Investigation, Data curation. **I.V. Yatsyk:** Investigation, Data curation. **A.S. Makarchenko:** Investigation, Data curation. **Yu.A. Deeva:** Resources, Investigation. **V.A. Shustov:** Investigation, Data curation. **D.I. Fazlizhanova:** Visualization, Investigation, Formal analysis. **R.M. Eremina:** Writing – review & editing, Validation, Supervision, Project administration, Methodology, Funding acquisition, Formal analysis, Data curation, Conceptualization.

Declaration of Competing Interest

The authors declare the following financial interests/personal relationships which may be considered as potential competing interests: Eremina R. reports financial support was provided by Russian Science Foundation. Maiti T. reports financial support was provided by India Ministry of Science & Technology Department of Science and Technology. If there are other authors, they declare that they have no known competing financial interests or personal relationships that could have appeared to influence the work reported in this paper.

Data Availability

Data will be made available on request.

Acknowledgments

This research was supported by the Russian Science Foundation (Project No. 22–42–02014) and the DST (Project No. DST/INT/RUS/RSF/P-55/2021).

References

[1] Z. Gui, et al., Adv. Sci. 10 (2023) 2303967.
[2] Y. Zheng, et al., Sci. Adv. 5 (2019) 9461.
[3] M.M.H. Polash, F. Mohaddes, M. Rasoulianboroujeni, D. Vashaee, J. Mater. Chem. 8 (12) (2020) 4049–4057.
[4] J. Endo, H. Matsuura, M. Ogata, Phys. Rev. B 105 (4) (2022) 045101.
[5] G. Blasse, J. Inorlg. Nucl. Chem. 27 (1965) 993–1003.
[6] K. Yoshii, J. Solid State Chem. 151 (2000) 294–297.
[7] R. Kumar, R.N. Bhowmik, A.K. Sinha, J. Alloy. Compd. 920 (2022) 165917.
[8] R. Kumar, R.N. Bhowmik, J. Phys. Chem. Solids 181 (2023) 111505.
[9] G.J. Wang, C.C. Wang, S.G. Huang, J. Wang, L.N. Liu, Ceram. Int. 40 (2014) 14607–14612.
[10] M. Saxena, T. Maiti, J. Alloy. Compd. 710 (2017) 472–478.
[11] M. Saxena, T. Maiti, Scr. Mater. 155 (2018) 85–88.
[12] S.A. Dar, R. Sharma, V. Srivastava, U.K. Sakalle, RSC Adv. 9 (17) (2019) 9522–9532.
[13] O. Sahnoun, H. Bouhani-Benziane, M. Sahnoun, M. Driz, J. Alloy. Compd. 714 (2017) 704–708.
[14] P. Giannozzi, et al., J. Phys.: Condens. Matter 21 (39) (2009) 395502.
[15] P. Giannozzi, et al., J. Phys.: Condens. Matter 29 (46) (2017) 465901.
[16] L.A. Agapito, S. Curtarolo, M.B. Nardelli, Phys. Rev. X 5 (1) (2015) 011006.
[17] A.R. Supka, et al., Comput. Mater. Sci. 136 (2017) 76–84.
[18] A.K. Azad, S.-G. Eriksson, S.A. Ivanov, R. Mathieu, P. Svedlindh, J. Eriksen, H. Rundlof, J. Alloy. Compd. 364 (2004) 77–82.
[19] M. Varghese, S. Simpson, G. Lawrence, M. Duttine, P. SanzCamacho, M. Gaudon, O. Toulemonde, J. Phys. Chem. C. 126 (19) (2022) 8450–8460.
[20] L. Siurakshina, B. Paulus, V. Yushankhai, E. Sivachenko, Eur. Phys. J. B 74 (1) (2010) 53–61.
[21] K. Oka, M. Azuma, Spin-Crossover Cobaltite: Review and Outlook, Springer Singapore, Singapore, 2021.
[22] D.V. Popov, R.G. Batulin, M.A. Cherosov, I.V. Yatsyk, T.I. Chupakhina, Y.A. Deeva, R.M. Eremina, T. Maiti, Magn. Reson. Solids 25 (3) (2024) 23301–23309.
[23] D. Gangwar, C. Rath, Phys. Chem. Chem. Phys. 22 (25) (2020) 14236–14245.
[24] D.V. Popov, T.P. Gavrilova, I.F. Gilmutdinov, M.A. Cherosov, V.A. Shustov, E. M. Moshkina, L.N. Bezmaternykh, R.M. Eremina, J. Phys. Chem. Solids 148 (2021) 109695.
[25] R.M. Eremina, Fiz. Tverd. Tela 39 (1997) 1320–1322.
[26] A. Abragam, B. Bleaney, Electron paramagnetic resonance of transition ions, OUP, Oxford, 2012.
[27] E. Colacio, J. Ruiz, E. Ruiz, E. Cremades, J. Krzystek, S. Carretta, J. Cano, T. Guidi, W. Wernsdorfer, E.K. Brechin, Angew. Chem. 125 (35) (2013) 9300–9304.
[28] J. Krzystek, S.A. Zvyagin, A. Ozarowski, A.T. Fiedler, T.C. Brunold, J. Telser, J. Am. Chem. Soc. 126 (7) (2004) 2148–2155.
[29] M.N. Sanz-Ortiz, F. Rodríguez, G. Demazeau, High. Press. Res. 28 (4) (2008) 571–576.
[30] I. Pallecchi, G. Lamura, G. Tropeano, M. Putti, R. Viennois, E. Giannini, D. van Der Marel, Phys. Rev. B 80 (21) (2009) 214511.
[31] G. Nazir, A. Rehman, S. Hussain, E. Algrafy, Q. Mahmood, A. Mera, H.H. Hegazy, S. Alharthi, M.A. Amin, Mater. Today Commun. 31 (2022) 103547.
[32] I. Yatsyk, R. Eremina, T. Chupakhina, Yu. Deeva, Magn. Reson. Solids 21 (2022) 22202.
[33] S. Ivanova, E. Zhecheva, R. Stoyanova, Phys. Status Solidi (a) 205 (7) (2008) 1685–1689.
[34] R. Stoyanova, A.L. Barra, E. Zhecheva, R. Alcantara, G. Ortiz, J.L. Tirado, Inorg. Chem. 48 (11) (2009) 4798–4805.